Metal Artifact Reduction in Computed Tomography

Project Report by

Matthew Goh, ———, ———, ———

Department of Electrical and Computer Engineering
EECE5664 Biomedical Signal Processing and Medical Imaging
Northeastern University
Spring 2017

Contents

1 Introduction

X-ray computed tomography (CT) is an essential technique used in biomedical applications to non-invasively produce cross-sectional images of organs, bone, soft tissue, and blood vessels. In comparison to other tomographic techniques, the projections in x-ray CT represent the attenutation of energy as an x-ray travels through biological tissue [4]. In order for the scanned object or anatomical structure to be visible, it must contain physical contrast (e.g. differences in density or chemical composition) relative to its surrounding tissue or medium [9]. The shade of gray in conventional 2D x-ray images correspond to repeated projection of 2D slices onto a line in the 2D image. X-ray-based CT is an extension of this concept which allows for the reconstruction of the 2D slice by collecting many projections at many rotation angles. This forward process is modeled mathematically by the Radon transform, and the corresponding inverse process used to reconstruct an image slice is known as Filtered Back Projection (FBP). In practice, these projection measurements can be acquired in many ways. Many modern CT scanners use a panel of digitally-connected photo detectors and a single fan-beam source mounted on a gantry which rotates to acquire different projection angles. Lines of response in this fan-beam-geometry data (sometimes referred to as a fanogram) can be reorganized or rebinned into parallel-beam-geometry data (referred to as a sinogram) which corresponds to the Radon transform mathematical model.

The FBP algorithms used to reconstruct images are based on the monochromaticity assumption of the x-ray source such that the sinogram is an approximation of the Radon transform of a material's attenuation coefficient distribution at a fixed energy level [8]. For most soft tissues in the body, this assumption is valid; however, if there is metal present in the structure, this assumption is violated because the attenuation coefficients of metallic materials vary greatly with energy level, thereby leading to a significant mismatch between the sinogram data and the Radon transform of the image. This causes 'star artifacts' in the reconstructed image that result in a loss of anatomical information. Metallic objects in patients often include dental implants, surgical clips, steel-hip prostheses, bullets, or shrapnel. An example of a star artifact in a head CT scan is shown in Figure 1 below.

Figure 1: Star artifact in scan of 50 year old male with gunshot wound. Reference: https://radiopaedia.org/articles/ct-artifacts

Reduction of these artifacts has been the topic of much effort in the field of medical imaging

[5, 10]. If an effective algorithm can be designed to remove these star artifacts, the quality of medical images can be dramatically improved for cases in which the scanned structure includes metal [8]. Specifically, this would allow for improved CT scans in patients with metal pins, clips, splints, shrapnel, bullets, or implanted medical devices.

The aim of this project was to study and compare several metal artifact reduction (MAR) methods. In our approach, we:

1. reviewed literature for preliminary background information and contextual knowledge
2. developed mathematical models and simulations for CT
    i. absorption-only (conventional) model
    ii. full absorption and scattering model
3. replicated existing algorithms for metal artifact reduction, and
4. evaluated and compared the performance of these algorithms using simulated data

Our literature review and mathematical models are presented in Sections 2 and 3.1 respectively. The algorithms ultimately selected for study and replication were 1) iterative sinogram interpolation and 2) gradient descent with image segmentation. Lastly, because image noise is a topic of concern in the study of MAR techniques, an investigation of image prefiltering methods used in combination with sinogram interpolation was also performed; this is presented in Section 3.3.

2 Literature Review on Metal Artifact Reduction

An article by Park et al (2014) provides a mathematical characterization and analysis of beam-hardening artifacts in X-ray CT scans [8]. It is found that metal artifacts can be reduced by gathering the tilted reconstructions of CT from multiple angles of the same object. The transverse CT slice that is gained by the tilted images could show less metallic objects which in turn reduces streaking artifacts. The mathematical characterization begins by giving the CT image reconstructed by FBP

$$f_{ct}(x) := \frac{1}{4\pi} R^* I^{-1} P(x)$$

where R^* is the adjoint Radon transform

$$R * h(x) = \int_{-\pi}^{\pi} h(\psi, x \cdot \theta) d\psi$$

and $I^{-1}g$ is the Riesz potential

$$I^{-1}g(s) = \frac{1}{2\pi} \int_R \int_R e^{i(s'-s)\omega} g(s') |\omega| ds' d\omega$$

It then moves on to express the distribution of the attenuation coefficient f_E,

$$f_E(x) = f_{E_0}(\psi, s) + \delta_{D,\alpha^{E_0}}(\psi, s) \sum_{j=1}^{N} \alpha_j^{E_0} R x_{D_j}(\psi, s)$$

It is found that in high energy CT, once the electron energy reaches and exceeds 100keV, the attenuation coefficients begin to plateau and variance with E decreases to approximately zero. In order to provide artifact-free CT images, it is necessary for $f_C T \approx f_{E_0}$. Upon adjusting the energy range to anywhere between 80keV to 150 keV, streaking artifacts in f_{CT} are extremely reduced because α_j is negligible under those conditions. A very important discovery was made when they realized that the metal streaking artifacts exist solely when generated by the drastic nonlinear mismatch of the projection data, P, that is dependent on the geometry of the high attenuation materials $U_{j=1}^{N} N D_j$. Microlocal analysis can then be used to concurrently determine the locations and orientations of singularities. Metal streaking artifacts are created by the extreme nonlinear mismatch of the projection data depending on the geometry of the high attenuation materials. In order to characterize the streaking artifacts mathematically, they must be confined to the wavefront set of straight line:

$$L_{\psi,s} = x = s(cos\psi, sin\psi) + t(-sin\psi, cos\psi) : t \in \mathbb{R}$$

The authors' analysis indicates that the streaking artifacts produced by the beam-hardening factor occur along the tangent line to ∂D, the boundary of D.

They determined that if region D is strictly convex or annulus then no tangent lines are touching two different points on the boundary of D so f_{CT} does not have streaking artifacts. If there are four tangent lines touching two different points on the boundary of D, there are streaking artifacts created in the reconstructed CT image by filtered back projection. This study is beneficial in the sense that it helps determine the locations and shapes of the implants inside the patient which helps reduce metal streak artifacts but there are problems presented by the fact that the inverse problem is nonlinear and depends highly on the geometry of the high attenuation objects. Using the knowledge that they have of metallic implant shapes, they believe that the opportunity to invent a novel artifact correction method depending highly on mathematical characterizations discussed above.

A paper by Yu et al (2007) discusses a segmentation-based interpolation method using surgical aneurysm clips to reduce the metal artifacts in CT scans [11]. The authors use a five step process for metal artifact reduction beginning with coarse image reconstruction using the full-scan filtered backprojection algorithm. The next steps are to segment the metallic object using computer vision mean-shift technique and then use forward projection of the characteristic image into the sinogram domain to obtain the intersectional length of the corresponding x-ray path associated with the metallic objects. Then projection interpolation begins by deleting the corrupted projection data from the original projection and then using the feedback interpolation strategy they were able to obtain a new interpolated projection. Finally, they used filtered backprojection from the interpolated projection and difference projection to reconstruct a background image and a metallic image.

The coarse image, $I_O(m, n)$, that is initially reconstructed is obtained from a fixed region of interest in which larger M and N values equate to smaller pixel size. Using mean-shift technique the metallic objects were extracted from I_O and the definition of characteristic image,

I_C, was determined to be

$$I_C(m,n) = \begin{cases} 1, & \text{if } I_o(m,n) \text{ belongs to metallic objects} \\ 0, & \text{otherwise} \end{cases} \tag{1}$$

I_C is then forward projected into the sinogram domain and allows them to obtain an index with the metallic objects and the corresponding pixels. The original projection data minus the corrupted projection data allows for a difference projection dataset to be produced that is completely formed by the metallic objects. The final image is consists of a scale factor, η, from 0.05 to 0.5 and a mask I_C^* that is the convoluted I_C and a normalized Gaussian kernel in order to protect the background image from corruption endured due to the metallic objects. The scaled scheme is defined as

$$I_F(m,n) = I_B(m,n) + \eta \times I_C^*(m,n) \times I_M(m,n)$$

There are various techniques in order to complete metallic object segmentation and the use of the mean-shift procedure is merely one of them. The novel idea to analyze a complex multimodal feature space using a nonparametric method and then to delineate clusters within it proved to be very effective and when applied managed to maintain smoothing and image segmentation. It is imperative that discontinuity is preserved. Mean-shift smoothing filtering follows these steps:

1. Initialize $l = 1$ and $y_{k,l} = x_k$
2. Compute $y_{k,l+1} = M_S(y_{k,l})$ until converging to the final result $y_{k,l}$
3. Assign the output $z_k = (x_k^s, y_{k,L}^r)$

At this point metallic object segmentation can be applied based on the fact that human tissue has lower attenuation than the metal artifacts so simple threshold method can be applied. The result had a morphological dilation used on it to make up for the blurring that was incurred due to the focal spot of the x-ray source. Using this method they were able to reduce metal artifacts by 20%–40% related to the standard deviations with soft tissues and osseous structures surrounding the metallic clips.

3 Methods and Results

3.1 CT Mathematical Modeling

Most methods for MAR require a numerical model for a CT scan as a prerequisite. For the purposes of this project, a simple 2D model was preferable. Most mathematical models for CT are based on a parallel-beam configuration, which describes the physical arrangement between the x-ray source and x-ray detector (see Figure 2). In parallel beam geometry, the lines-of-response are determined by a rotation angle θ and a projection shift position l. For a fixed θ and lateral position l of the beam, the value $g(l,\theta)$ is called the projection of the scanned cross-sectional image, and for all values of l and θ, $g(l,\theta)$ is defined as the 2-D Radon transform of an image $f(x,y)$:

$$g(l,\theta) = \int_{-\infty}^{\infty} \int_{-\infty}^{\infty} f(x,y)\delta(xcos\theta + ysin\theta - l)dxdy$$

where x and y are rectilinear coordinates on a 2-D plane and δ is the 1-D Dirac delta function [3].

However, because fan-beam collimation is the more typical configuration in real CT scanners, our mathematical model assumes fan-beam geometry (see Figure 3) in order to provide a more realistic simulation. In Figure 3, the parameter γ is the angular position of a given detector, and β is the angular position of the source, both of which are measured from the counterclockwise direction. The parameters l and θ as in the parallel-beam case can be related to the new fan-beam parameters by $\theta = \beta + \gamma$ and $l = Dsin\gamma$, where D is the distance from the source to rotational isocenter. Examples of fan-beam vs. parallel-beam CT geometry are shown in the figures below.

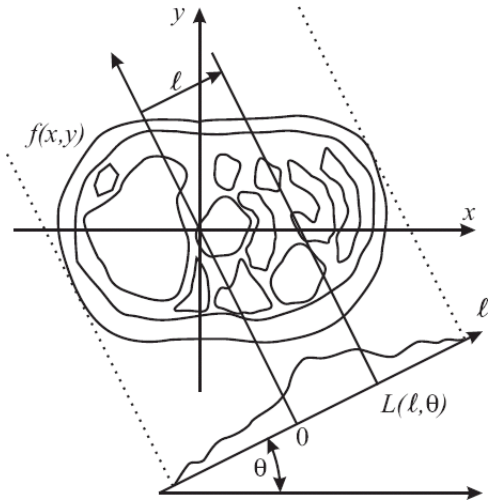

Figure 2: A parallel-beam CT scan. The parameters of interest are the projection angle θ and the lateral position l. Reference: Prince and Links (2004)

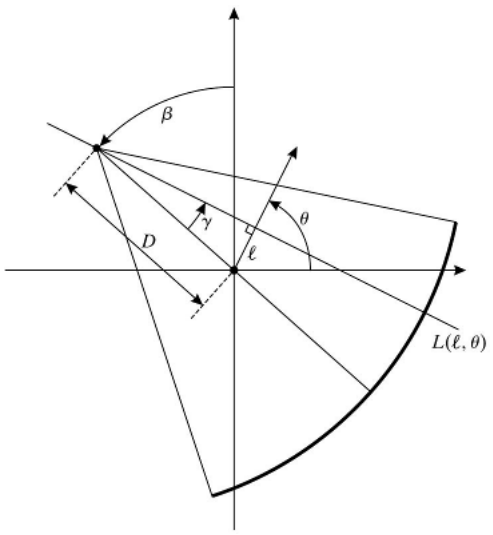

Figure 3: A fan-beam CT scan. The parameters of interest are the fixed source-to-center distance D, the projection angle θ and the lateral position l. Reference: Prince and Links (2004)

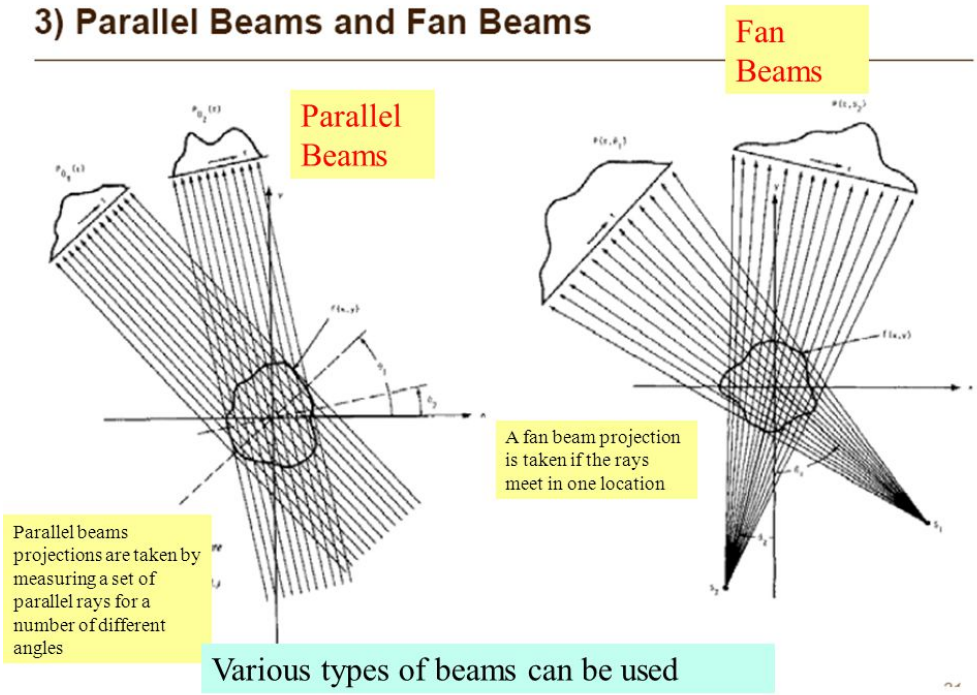

Figure 4: Images showing a direct comparison between parallel-beam and fan-beam CT configurations. Reference: Amos Collins "Data Acquisition, Representation and Reconstruction of medical images Application of Advanced Spectral Methods." http://slideplayer.com/slide/4261749/

For our project, a simple 2D fan-beam model was generated from scratch. A function was written to build a scan geometry structure which contains all the important parameters and meshgrids for the imaging tasks. Another piece of code was written to generate a forward projection matrix `F`. The use of `F` is shown in the equation

$$\mathrm{f} = \mathrm{F} \times \mu,$$

where μ is an (N $\times$ 1) column vector representing the pixel-grid of x-ray attenuation coefficients (μ) in x-y space, `f` is an (M x 1) column vector representing the pixel-grid of measured space-integrated x-ray attenuation coefficients (g-values) in fanogram-space (view angle $\times$ fan angle), and `F` is an (M x N) forward projection matrix which transforms an image into the fanogram measurements that would be collected for that image. The algorithm used to generate `F` was very slow since `F` is a large matrix (`40401` $\times$ `40401`) and must be organized as a MATLAB sparse matrix to save space. Each line of response is treated as an ideal line in two dimensions which passes through the x-y image space which is broken up into pixel basis functions. `F(i,j)` is therefore proportional to the total distance that the `i`'th line of response travels in the `j`'th pixel. The resolution of the forward projector is determined by the image resolution `N` and the fanogram resolution `M`. If an object is smaller than the size of a pixel in image space, there will be partial volume effects when that region is down-sampled to match the forward projector. Since the fanogram and sinogram are both made up of g-values, the fanogram can be re-binned by computing the sinogram parameters `(s,phi)` for each pixel in the fanogram image and using a scattered linear interpolant onto an evenly-spaced grid in sinogram-space. Once the sinogram was computed, MATLAB's `iradon` CT reconstruction algorithm was used to recover

a reconstructed estimate of μ. Representations of the Shepp-Logan phantom in all relevant imaging spaces are shown below.

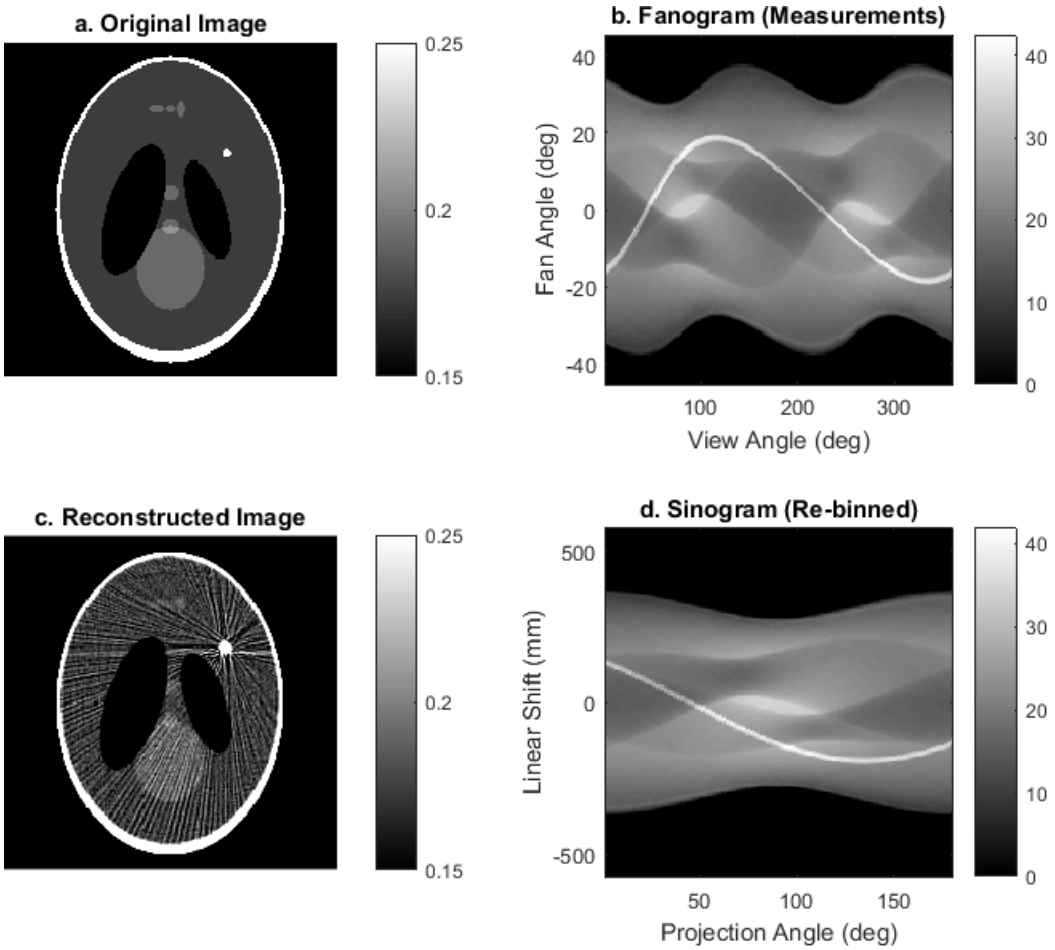

Figure 5: The original 2D image in x-y-space (top left), the synthetic measurements collected by a simulated scanner in fanogram-space (top-right), the measurements re-binned into sinogram-space (bottom right), and the reconstructed image generated by applying MATLAB's iradon to the sinogram (bottom left).

Scattering effects where not included in the mathematical model because the dominant physical process which leads to star artifacts is simply attenuation. When the attenuation is too high, the signal-to-quantization-noise goes down resulting in star-artifacts.

3.2 Sinogram Interpolation Algorithm

The sinogram interpolation algorithm is based on the algorithm described in the paper "A New Method for Metal Artifact Reduction" [6]. In this algorithm, the first step is to generate an initial image from the original projections just like any other CT image reconstruction algorithm. The filtered backprojection will produce an image with artifacts which look like stars radiating from the metal object. The purpose of this algorithm is to remove the artifacts in sinogram space and then backproject to remove the star artifacts.

To begin the artifact removal, the metal piece was first isolated by thresholding pixels with intensities greater than 30% of the maximum intensity value in the image. The 30% threshold

was chosen because it isolated the most metal while excluding all non-metal materials. The next step was to take the Radon transform of the new metal-only thresholded image which produced the metal-only image in sinogram space. The metal-only image and metal-only sinogram can be seen in Figure 6 below.

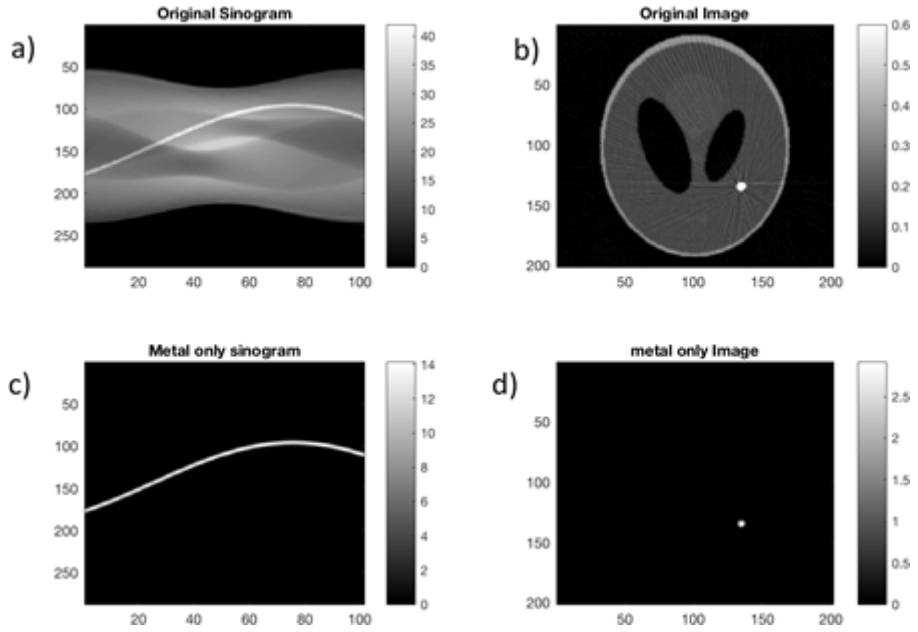

Figure 6: a) The original sinogram generated from the 2D CT simulator. b) The original image created by taking a filtered back projection of the original sinogram. c) The metal only sinogram generated by taking the Radon transform of the metal only image. d) The metal only image which was created by a threshold of the original image

The new metal sinogram was used as a mask to remove metal from the original sinogram. The metal replacement step was the most important and difficult part of the algorithm to perform because there were multiple methods available to interpolate across the gap that was made when the metal was temporarily removed. The method of interpolating the data was the scattered interpolation function in MATLAB for two dimensional image interpolation. There are three different types of interpolation methods for this built in function, linear interpolation, natural interpolation and nearest interpolation. The images in Figure 7 show the sinogram when the metal was removed before interpolation and then when it was interpolated using the natural method.

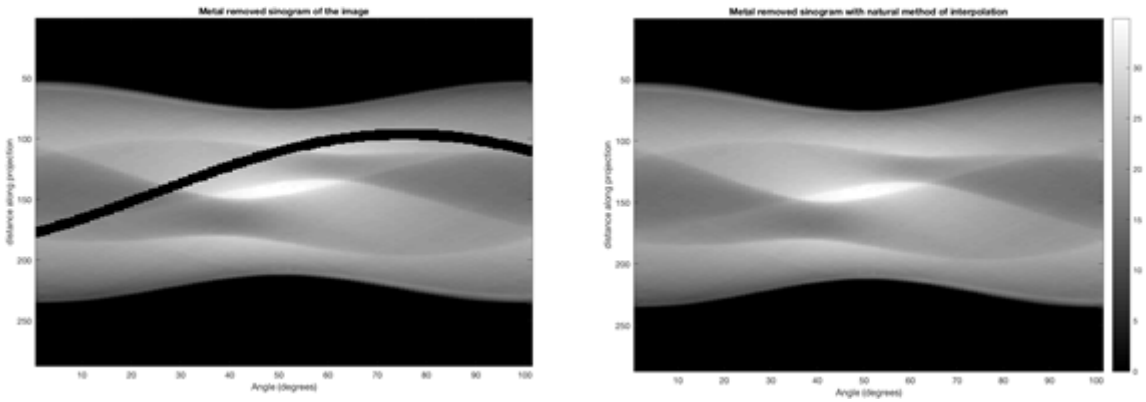

Figure 7: The sinogram on the left shows the image when the metal was removed. The image on the right shows the image when the empty space was interpolated.

The natural interpolation for the sinogram interpolation with a Ram-Lak filtered back projection with linear interpolations for the inverse Radon transform were used for the image reconstruction in the first step of the algorithm described in the paper. The natural interpolation method for the scatted 2D interpolation was chosen because it provided the best results. This method used the Deluanay triangulation method for interpolation and produced much smoother interpolation than the other options. The first metal artifact reduction image can be seen below which shows the metal artifacts removed from the image and the actual metal is still present but the underlying data is not disturbed by the metal streaks.

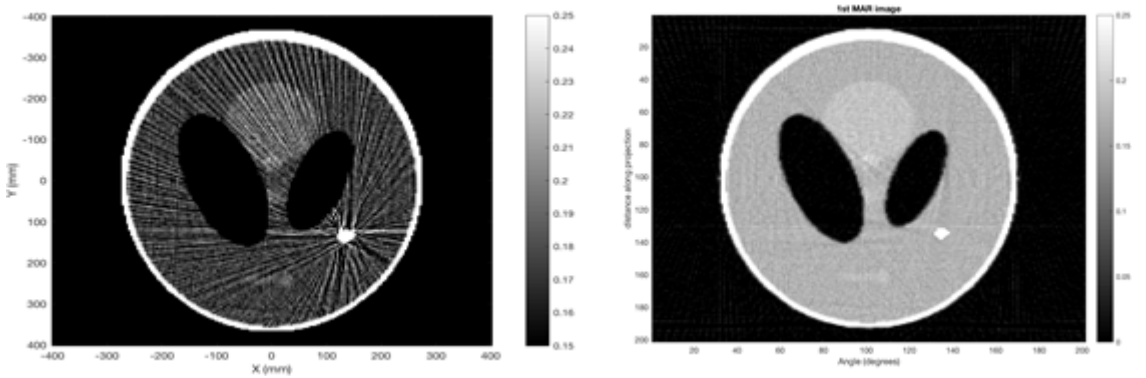

Figure 8: The first metal artifact reduction image, on the right, clearly removes the metal star artifacts from the image and produces the first MAR image. The original image can be seen on the left for comparison.

The first MAR image sufficiently removes the star artifacts for this specific example to be the final result of this algorithm, but the paper mentioned at the beginning of this subsection added a segmentation step in order to remove the artifacts further that the first step could not remove. The issues that still remain with the reconstructed image are that there is not much contrast between some of the objects in the original image that existed. For example, the faded circle between the two black ellipses was more prominent in the first MAR image. The paper mentions that the following steps could be iterated multiple times to further reduce artifacts. In the segmentation step, the various types of materials in the first MAR image are characterized and thresholds are found by visually inspecting the histogram of pixel space to classify the materials in the sinogram. The ranges of pixel values for each material are averaged together and all pixels in the range are replaced by the average value. The thresholds were chosen

by using a histogram that will peak at the mean value for each material in the image and the minimums between each peaks would act as a threshold. In this implementation, the thresholds were chosen manually by visually inspecting the histogram, but it could be automated. In this case there were three peaks and the histogram for the first MAR image can be seen in Figure 9.

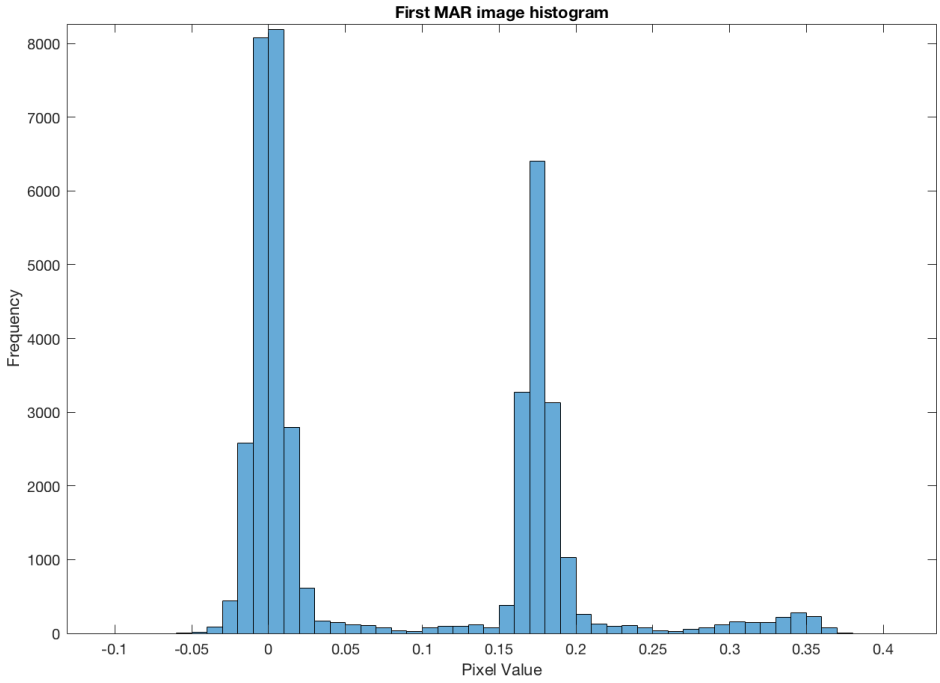

Figure 9: Histogram used to find the pixel threshold values for the different materials.

The goal of the segmented image was to find a correction image that could be subtracted from the original image in order to remove the metal artifacts as well. This was a separate technique that needed the first MAR image from the sinogram interpolation in order to find a better segmented image. The segmented image and segmented sinogram generated from the thresholds can be seen below in Figure 10.

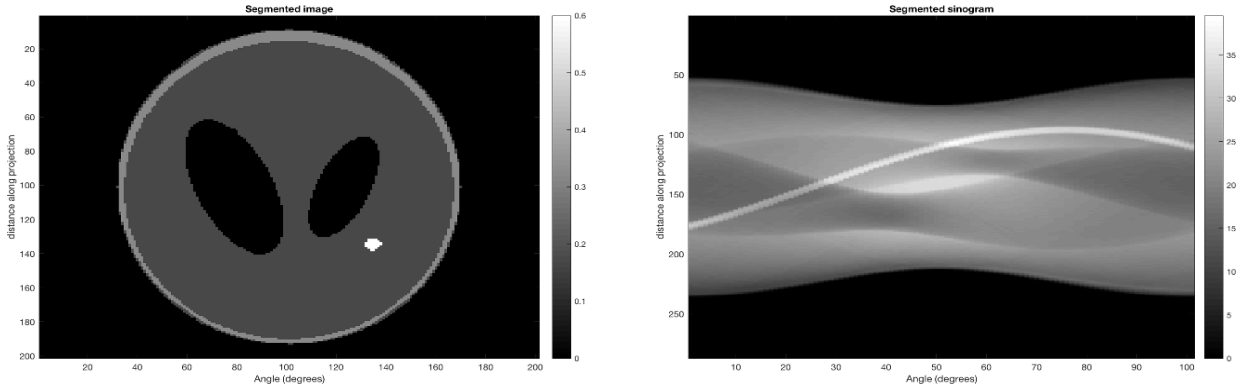

Figure 10: The image generated from the segmentation through thresholding and the sinogram generated by taking the Radon transform of the image.

The segmentation sinogram was subtracted from the original sinogram to create an error sinogram. The difference between the original and the segmented one show some of the high frequency errors that still exist in the image. The errors created specifically by the metal were

recreated by using the metal mask from the previous step to isolate the errors created by the metal which created the correction sinogram. The correction sinogram was backprojected in order to create the correction image. The correction image was subtracted from the original image in order to get an even more filtered image. The error sinogram and correction image can be seen in Figure 11.

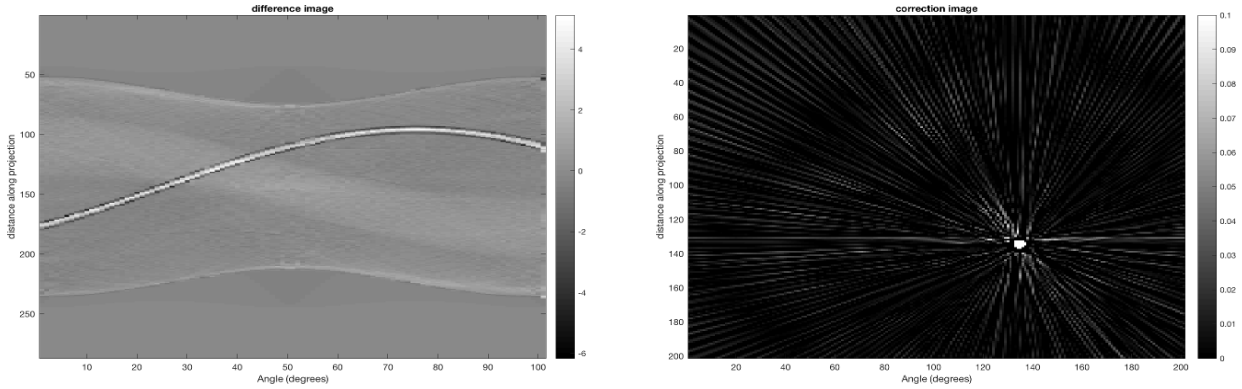

Figure 11: The error sinogram, on the left, generated from the difference between the original and segmented sinograms. The correction image can be seen on the right which shows the star artifacts that were removed.

The correction image was then subtracted from the original image in order to remove the artifacts from the image. The second MAR image can be seen in Figure 12.

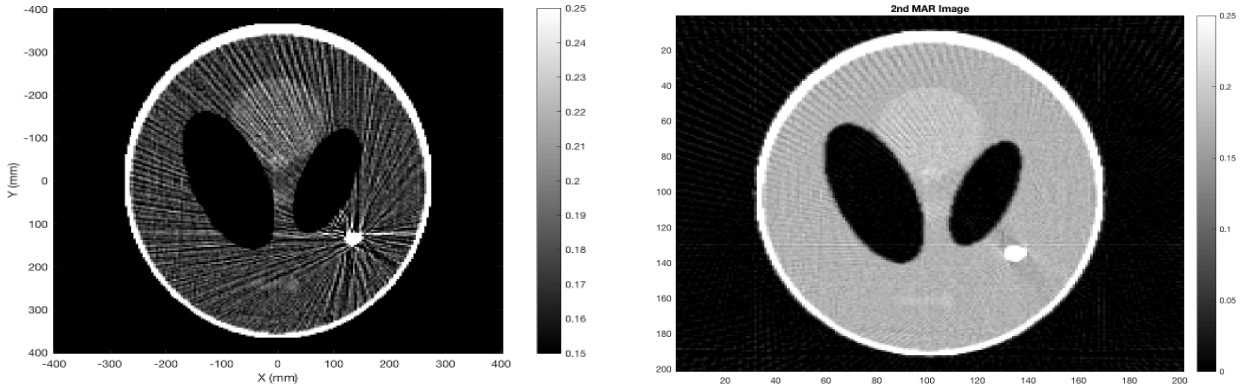

Figure 12: The second MAR image (right) shows a large reduction in the star artifacts created from the metal artifacts in the original image on the left.

The second MAR image can be used as input to the beginning of the second part of this algorithm and iterated over again to get a third MAR image as output. Then the output can be used as input again as many times as needed to get rid of the artifacts further. The image based least squared cost was calculated using the original image to see how closely the image was reconstructed by comparing the new value to the value from the initial image without filtering. The equation for the image-based least squared error cost is:

$$Cost = \sum (\mu - \hat{\mu})^2$$

where μ is the 'ground truth' noise-less phantom and $\hat{\mu}$ is the MAR image.

The cost of the initial image calculated using the equation is 2461.7 directly after reconstruction. The cost of the first MAR image is 32.82 and the cost of the second MAR image is 69.29. Therefore, the first MAR image is a closer representation of the original image than the second MAR image. The least squared error cost is a good measure of the reduction of the artifacts because the it compares the differences between the initial image and the filtered image. The comparisons between the two filtered images and the respective cost values show that there are visual differences proportional to the cost values. The first MAR image has less artifacts than the second MAR image and the first cost value is less than the second cost value. The cost values make sense in this implementation and represent the results accurately.

3.3 Sinogram Interpolation Using Non-local Means Prefiltering

Because the nature of x-ray CT contains ionizing radiation, a guiding principle in CT clinical practice is to minimize radiation dose levels while maintaining acceptable diagnostic accuracy. However, the trade off for lowering radiation dose alone is a noisier image, which may degrade diagnostic performance or undermine physician confidence [7]. Therefore, this contextual knowledge served as a motivation to explore image prefiltering techniques.

A paper by Chen et al proposed a method of MAR whereby the initial image is first edge-enhanced using a non-local means filter, which is an effective image denoising strategy that exploits the inherent self-similarity present in nearby image patches [1] . This allows NLM to preserve a high degree of image texture and fine detail [7]. In the paper by Chen et al, the metallic objects are extracted from the rest of the image, forward projected into sinogram space, and subtracted from the original sinogram data. The missing projection data is then restored using a method similar to the sinogram interpolation method described in the previous subsection. In summary, the steps were:

1. Prefiltering of the original CT image using an edge-preserving non-local means (NLM) filter.

2. Image segmentation of the metal artifacts and objects using a mutual information maximized segmentation (MIMS) algorithm.

3. Sinogram interpolation of the subtracted sinogram

4. Filtered backprojection to produce a final image

For this study, a MATLAB implementation of the NLM filter was applied to the Shepp-Logan phantom with the added star artifact and with Gaussian white noise. Because our simulated metal artifact and object is relatively simplistic, it was not necessary to employ the MIMS segmentation algorithm described in Chen et al. Instead, the thresholding technique described in the previous subsection was used to segment the metal object.

As previously stated, the goal of the NLM filter is to denoise the image and improve edge contrast between the metal object and the surrounding tissue. Given a noisy image $v = v(i)|i \in I$, the estimated value $NL[v](i)$ for each pixel i is the weighted average of all the pixels in the image:

$$NL[v](i) = \sum_{j \in I} w(i,j)v(j)$$

where the weights $w(i,j)$ depend on the similarity between the neighborhoods of pixels i and j. Furthermore, the weights $w(i,j)$ satisfy the conditions $0 \leq w(i,j) \leq 1$ and $\sum_j w(i,j) = 1$.

The similarity between two pixels i and j are based on the weighted Euclidean distance:

$$||v(N_i) - v(N_j)||_{2,a}^2$$

where $a > 0$ is the standard deviation of the Gaussian kernel and N_i is the square neighborhood centered about pixel i defined by a radius similarity window R_{sim}. The weights are then calculated using the equation

$$w(i,j) = \frac{1}{Z(i)} \, e^{-\frac{||v(N_i)-v(N_j)||_{2,a}^2}{h^2}}$$

where $Z(i)$ is the normalizing constant

$$Z(i) = \sum_j e^{-\frac{||v(N_i)-v(N_j)||_{2,a}^2}{h^2}}$$

and h is the weight-decay parameter that controls the amount of denoising performed. Values of h that are set too low will not remove enough noise, and h values that are set too high will result in blurrier images.

The initial noisy Shepp-Logan phantom with the star artifact and the initial prefiltered image are shown in Figures 13 and 14, respectively, below.

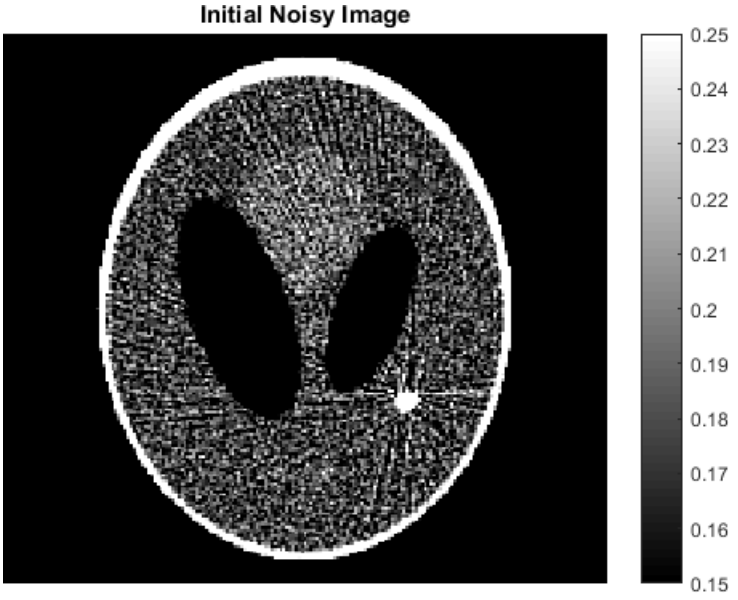

Figure 13: Initial Shepp-Logan phantom with star artifact and additive Gaussian noise

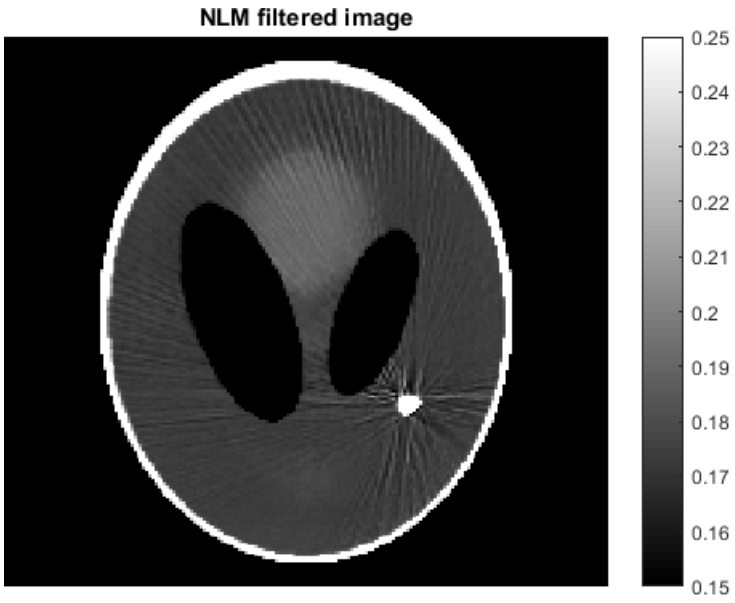

Figure 14: Initial NLM-filtered image

The NLM parameters (weight-decay, similarity window, neighborhood size) were optimized by selecting the values that produced the lowest least-squared error cost relative to the 'ground truth' image (Figure 5a), and through visual inspection. The latter was necessary because, in some cases, the 'optimal' value based on lowest cost resulted in an undesired loss of information in the prefiltered image. An example of such a case is demonstrated in Figure 15 below.

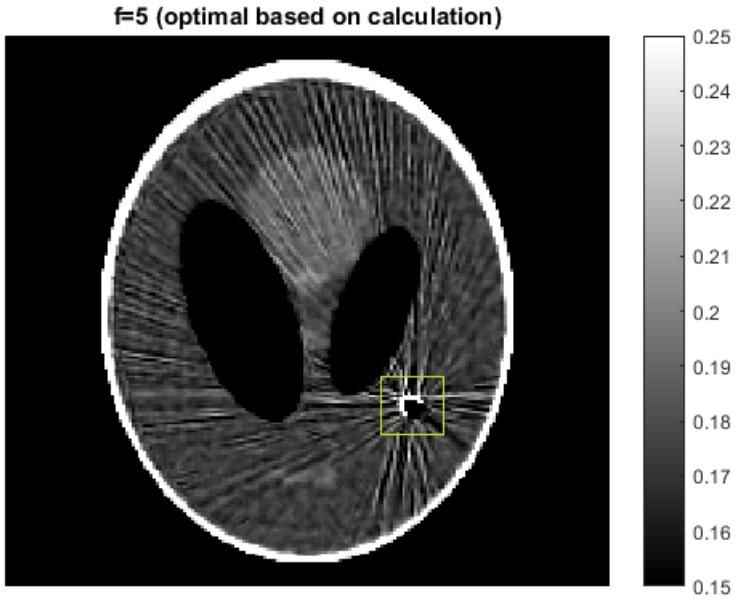

Figure 15: The optimal similarity window value (f=5) as computed based on least-squared error cost resulted in missing data in the metal artifact region, as indicated by the green square.

The last step was to then apply the sinogram interpolation method described in the previous subsection to the prefiltered image (Figure 14). The final result is shown in Figure 16 below.

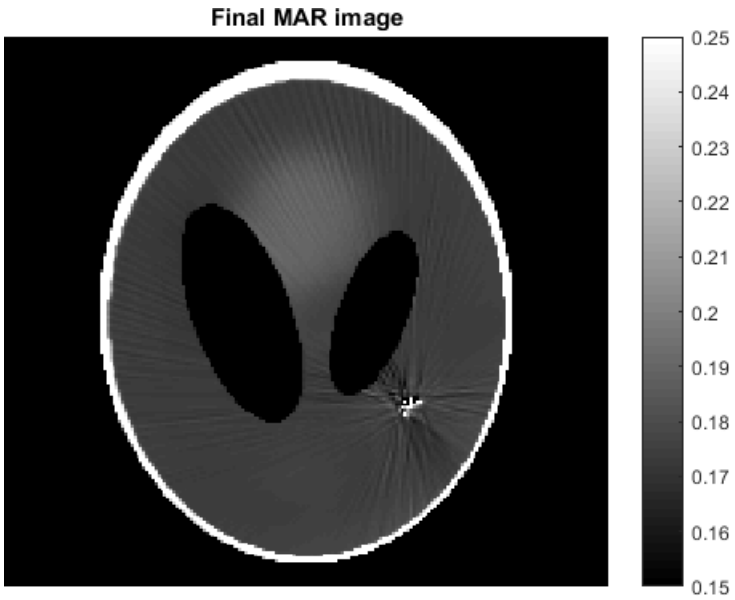

Figure 16: Final MAR image with NLM prefiltering and sinogram interpolation

The least squared error cost for the prefiltered image was computed to be 30.01, and the cost for the final sinogram interpolation image was computed to be 67.74. From this standpoint, it is unclear why the quality of the sinogram interpolated image (Figure 16) is poorer compared to the prefiltered image (Figure 14). Although Figure 16 appears to contain less 'streaks' from the star artifact, some of the metal has also been undesirably removed. This suggests that perhaps the NLM parameter values need to be improved, or that the thresholding step in the sinogram interpolation process needs to be reevaluated. It is worth noting that our model here contains only a single 2D image slice; a more thorough study could be performed if a full 3D model were used instead. Nonetheless, the results here demonstrate the efficacy of NLM prefiltering and sinogram interpolation.

3.4 Gradient Descent with Image Segmentation

This section will discuss an approach which treats image reconstruction as an optimization problem [2]. The goal of these algorithms is to minimize a data-based least-squared function given by

$$J = \sum_i (g_i - (T\mu)_i))^2$$

where J is the least-squared cost, g is the measured sinogram data, μ is a hypothesized X-ray mass attenuation coefficient distribution. The capital T represents a forward projection operator. Therefore, the parenthetical expression where T acts on μ is defined in the same sinogram space as the measurements. The least-squared cost function therefore represents the "goodness-of-fit" between a hypothesized image and the measured data. The solution to the reconstruction problem is therefore defined as the distribution which minimizes the least-squared cost or, in other words, matches the measured data most precisely given the forward model described by T.

In general, this sort of optimization problem is addressed with numerical optimization techniques such as gradient descent, Newton's method, and conjugate gradient. This section will consider a modified version of gradient descent. In this method, a gradient direction must be established. In other words, there must be a mathematical model which gives the small

change in the hypothesized contrast distribution which will lead to the steepest descent in the least-squared cost function. In this case, the model comes directly from the Radon transform: the model for CT scanners in general. It can be shown that the gradient direction is given by the following formulas:

$$\Delta g = g - T\ \mu$$

$$\Delta \mu = T^{-1} \Delta g = T^{-1}\ (g - T\mu)$$

If there are N pixels in the 2D distribution $\mu(x, y)$, then the least-squared cost is essentially a function of N variables – the values for each pixel in the image. For example, if an image is 100×100 pixels, then the optimization problem will involve a 10,000-dimensional feature space. In order for these problems to be computationally tractable, they usually take advantage of some a priori knowledge about the measurements or the subject under test. The effect of this is to reduce the search-space for the optimization problem. In this particular application, it is known that there is a human head under test with a possible metal inclusion. That means that the only material involved in the solution should be gray matter, white matter, air, bone, and possibly a metal inclusion. These restrictions can significantly speed-up computation time and increase accuracy.

The proposed approach is to mix a gradient-descent approach with image segmentation. At each iteration of gradient descent, the image will be segmented into metal, bone, air, and brain matter before continuing. The segmentation is performed by simply rounding to the nearest allowed value. The process follows the diagram shown below.

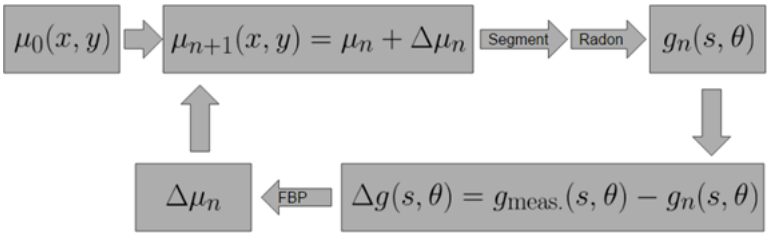

Figure 17

As previously mentioned, the ground truth for this numerical experiment is a Shepp-Logan numerical phantom (see Figure 5a). The initial guess for this algorithm was taken to be the straight-forward filtered back-projection algorithm that suffers severely from a metal artifact (see Figure 5c). The figure shows a clear metal star artifact centered on the metal inclusion. The details in the other ellipses are almost completely overwhelmed. Using the gradient descent with segmentation algorithm, the metal inclusion is isolated and segmented as well as the air, the bone, and the brain matter. An intermediate result and the final result is shown in Figures 18 and 19 respectively.

Figure 18

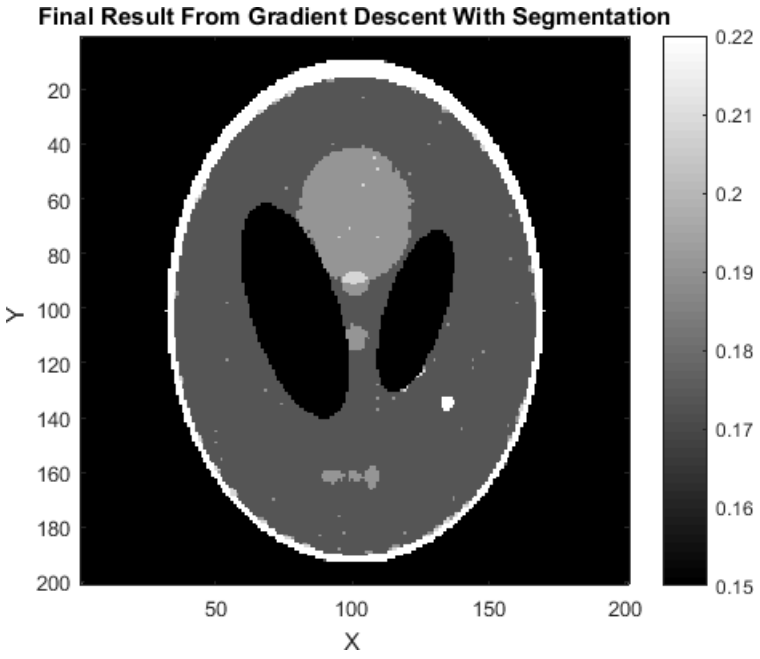

Figure 19

This final result appears to be a successful reconstruction of the ground-truth image. The metal inclusion is clearly shown and the details in the other ellipses can be clearly seen. The least-squared cost descent plot shown below shows that the cost converges as the gradient descent iterations progress.

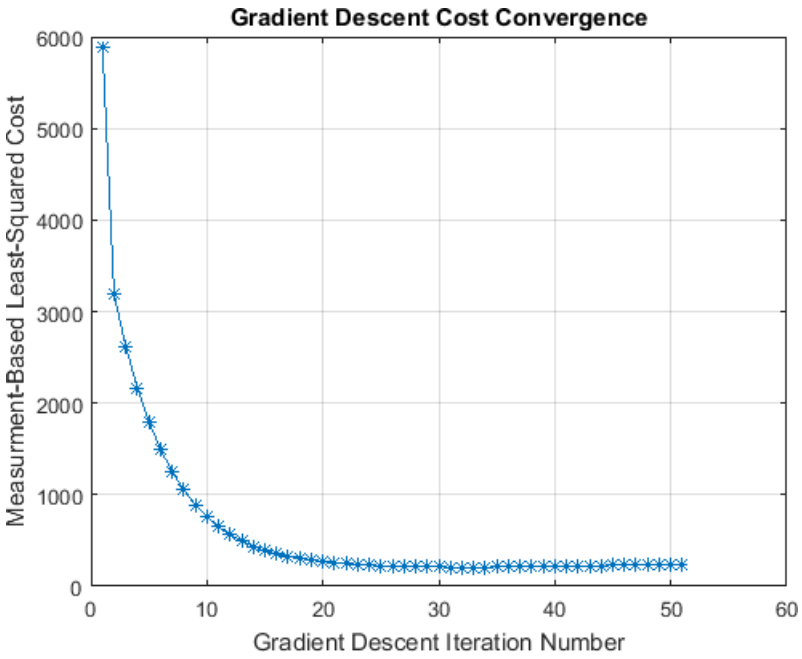

Figure 20

The image-based least-squared cost is 1.89 which is relatively low compared to the other approaches. This may be because this method took advantage of more a priori knowledge than the others.

4 Conclusions

From our literature review, it is clear that a variety of methods have been effective in reducing metal artifacts. The review on mathematical characterizations of methods such as beam hardening allowed us to further understand concepts such as filtered back projection, as well as the equations that represent streaking artifacts [8].

In evaluating the three approaches we implemented here (sinogram interpolation, sinogram interpolation with NLM prefiltering, gradient descent), it is important to consider the trade-off between performance and generality. Often, algorithms can be tuned to solve a particular problem very well at the expense of its ability to solve new and different problems in the future. This is analogous to the concept of over-fitting vs under-fitting in pattern recognition.

The gradient descent with segmentation approach exhibited the best performance of the three methods. However, it takes advantage of *a priori* assumptions that the others do not. This suggests that the other methods may be more generally applicable, for instance, to images of other parts of the body. By contrast, the gradient descent implementation is tuned specifically to segment brain tissue. If the application were known to be neuroimaging and the *a priori* assumptions for this algorithm were known to be valid, this is likely the best approach.

For further analyses and comparisons of the methods here, a sensible next step would be to apply these methods to 3D CT models, as well as to real CT data where voxel intensity inhomogeneities are much more prominent and the exact composition of the metal may be less certain.

Bibliography

[1] Y. Chen, Y. Li, H. Guo, Y. Hu, L. Luo, X. Yin, J. Gu, and C. Toumoulin. CT Metal Artifact Reduction Method Based on Improved Image Segmentation and Sinogram In-Painting. *Mathematical Problems in Engineering*, 2012. doi: doi:10.1155/2012/786281.

[2] O. Dorn and D. Lesselier. Level Set Techniques For Structural Inversion In Medical Imaging. *Topics in Biomedical Engineering. International Book Series*, pages 61–90, 2007.

[3] T. G. Feeman. *The Mathematics of Medical Imaging.* Springer, 2010.

[4] A. C. Kak and M. Slaney. *Principles of Computerized Tomographic Imaging.* IEEE, 1988.

[5] W. Kalender, R. Hebel, and J. Ebersberger. Reduction of CT artifacts caused by metallic implants. *Radiology*, 1987. doi: 10.1148/radiology.164.2.3602406.

[6] T. Koehler, B. Brendel, and K. M. Brown. A new method for metal artifact reduction. In *The Second International Conference on Image Formation in X-ray Computed Tomography*, 2012.

[7] Z. Li, L. Yu, J. D. Trzasko, D. S. Lake, D. J. Blezek, J. G. Fletcher, C. H. McCollough, and A. Manduca. Adaptive nonlocal means filtering based on local noise level for CT denoising. *Med. Phys.*, 41, 2014.

[8] H. S. Park, Y. E. Chung, and J. K. Seo. Computed tomographic beam-hardening artefacts: mathematical characterization and analysis. *Philosophical Transactions*, 2014. doi: 10.1007/s00330-004-2263-y.

[9] P. Sprawls. *The Physical Principles of Medical Imaging, 2nd Ed.* Medical Physics Publishing, Madison, Wisconsin, 1995.

[10] O. Watzke and W. A. Kalender. A pragmatic approach to metal artifact reduction in CT: merging of metal artifact reduced images. *European Radiology*, 14(5), 2004. doi: 10.1007/s00330-004-2263-y.

[11] H. Yu, K. Zeng, D. K. Bharkhada, G. Wang, M. T. Madsen, O. Saba, B. Policeni, M. A. Howard, and W. R. Smoker. A segmentation-based method for metal artifact reduction. *Academic Radiology*, 14(4), 2007. doi: 10.1016/j.acra.2006.12.015.